

Direct Visual Servoing Based on Discrete Orthogonal Moments

Yuhan Chen¹, Max Q.-H. Meng¹, Li Liu^{2,*}

Abstract—This paper proposes a new approach to achieve direct visual servoing (DVS) based on discrete orthogonal moments (DOM). DVS is performed in such a way that the extraction of geometric primitives, matching, and tracking steps in the conventional feature-based visual servoing pipeline can be bypassed. Although DVS enables highly precise positioning, it suffers from a limited convergence domain and poor robustness due to the extreme nonlinearity of the cost function to be minimized and the presence of redundant data between visual features. To tackle these issues, we propose a generic and augmented framework that considers DOM as visual features. By using the Tchebichef, Krawtchouk, and Hahn moments as examples, we not only present the strategies for adaptively tuning the parameters and order of the visual features, but also exhibit an analytical formulation of the associated interaction matrix. Simulations demonstrate the robustness and accuracy of our approach, as well as its advantages over state-of-the-art. Real-world experiments have also been performed to validate the effectiveness of our approach.

Index Terms—Direct visual servoing, Discrete orthogonal moments, Tchebichef moments, Krawtchouk moments, Hahn moments.

I. INTRODUCTION

VISUAL servoing (VS) refers to the use of the vision sensor data to control the motion of a robot [1]. In a typical VS pipeline, two closely linked themes are subjects of active research [2]: the design of visual features associated with the robotic task to be realized, and the control scheme with the chosen visual features such that the desired features are obtained during VS. The latter adopts the control scheme of ensuring an exponential decoupled decrease in error. The former employs the geometric primitives (points, straight lines, ellipses, and cylinders) as the visual features in image-based VS [3]–[5] or reconstructs the camera pose from geometric primitives as inputs for position-based VS [6]–[9]. The above approaches subject the image stream to an ensemble of measurement processes, including image processing, feature matching, and visual tracking steps, from which the visual features are determined [10]. Alternatively, a current method that bypasses these steps, namely Direct Visual Servoing (DVS), has been proposed over decade [11], [12]. It simply employs the luminosity intensity of the overall image to perform the VS pipeline. The DVS technique has shown highly accurate positioning even for approximated depths, partial occlusions, specular, and low-textured environments.

Nevertheless, it suffers from a limited convergence domain and poor robustness due to the extreme nonlinearity of the cost function to be minimized and the presence of redundant data between visual features.

Several methods have been reported to enhance the performance of the DVS approach, which are generally divided into two categories: learning-based methods and model-based methods. Typical learning-based DVS methods are presented in [13] and [14]. The scheme proposed in [13] is to project the image onto an orthogonal basis derived from the Principal Component Analysis (PCA) algorithm. More recently, [14] developed a novel framework to perform VS in the latent space learned from a convolutional autoencoder (AE). AE has been revealed for its ability to compress the redundant information into a compact code with better reconstruction than the PCA-based techniques. However, these methods involve an offline learning process, e.g., [13] and [14] require learning the eigenspace and the encoded information, respectively. Instead, the model-based VS methods can bypass the offline learning process, and they include algorithms based on histogram [15], [16], photometric Gaussian mixtures (PGM) [17], and Discrete Cosine Transform (DCT) [18], etc. All these methods extract global features by directly calculating the luminosity intensities of the overall image, and have demonstrated superior VS results. Specifically, [15] reported an approach that considers histogram as visual features. However, the method depicted in [16] can converge successfully with a faster convergence rate than that of [15]. However, the robustness of the proposed method in [16] is to be investigated. The methods proposed in [17] and [18] can solve this problem. The objective of PGM-based VS (PGM-VS) [17] is to minimize the difference between the desired Gaussian mixture and the Gaussian mixture computed from the current image varying over time. Although the robustness of this method has been demonstrated in numerous experiments, the key parameters λ_{gi} in the method rely heavily on empirical determinations, which limits its application. The method presented in [18] is to transform, via the DCT, the image from the spatial to the frequency domain, and then use the coefficients of the DCT to establish a new control law. The DCT is a discrete orthogonal basis, which is reasonably useful for image compression and filtering. Hence, the DCT-based VS (DCT-VS) has higher robustness; nevertheless, this technique is not flexible enough such that it can only consider global features without focusing on local information. In other words, it cannot be adjusted adaptively according to the various images. Therefore, we are going to propose a VS scheme with a large convergence region, strong robustness, and flexible parameter selection.

¹ Department of Electronics and Electrical Engineering, Southern University of Science and Technology, Shenzhen, China

² Department of Electronics and Electrical Engineering, The Chinese University of Hong Kong, Hong Kong, China

Inspired by DCT-VS, we propose a generic and augmented DVS framework by taking discrete orthogonal moments (DOM) as visual features into consideration. Strictly speaking, both DCT and PCA belong to the subclass DOM. It is well noted that there is a large amount of redundant data between neighboring pixels, which can be effectively eliminated by orthogonal moments; however, the computation of continuous orthogonal moments, such as Legendre and Zernike [19], requires a coordinate transformation and a suitable approximation of the continuous integrals, thereby leading to further computational complexity and discretization errors [20]. This is because DOM is able to sufficiently address the above issues, such that they are employed to represent visual features. It is found by the analysis that moments that are orthogonalized on a uniform lattice and fall within a limited discrete domain are more suitable for VS, such as Tchebichef (Chebyshev), Krawtchouk and Hahn moments (TM, KM and HM). Such three types of moments have similar properties to DCT. In particular, HM is more flexible in parameter tuning to take into account both global features and local information.

The main contributions of this paper are as follows:

- we propose a generic and augmented DVS framework by considering DOM as visual features, and provide an approach to calculate the order of moments in the VS;
- we present an analytical formulation of the associated interaction matrix;
- we indicate how to determine the relevant parameters when KM and HM are utilized for VS;
- we confirm through various simulations and robotic VS experiments that these methods allow for large displacements and a satisfactory decrease of the error norm.

The rest of the paper is organized in the following manner. Section II presents the formulation of the DOM and the associated VS features. Section III provides an adaptive selection of the associated parameters for KM and HM when employed as visual features. The order of DOM is also investigated when it is used as visual features. Afterwards, Section IV elaborates the derivation of the interaction matrix related to the DOM feature. Subsequently, Section V validates the DOM-based VS control scheme through various experiments conducted on both simulations and a real robotic arm platform. Finally, conclusions and future work are given in Section VI.

II. DOM AS VISUAL FEATURES

A set of DOM computed from a digital image represents the global characteristics of the image shape and exhibits a large amount of information regarding the different geometric features of the image [21]. Therefore, this section elaborates the DOM representation of DVS as visual features. Sections II-A and II-B review the definitions and computations of the discrete orthogonal polynomials, namely Tchebichef, Krawtchouk, and Hahn polynomials, respectively. Then, Section II-C introduces the relations between these three polynomials. Finally, Section II-D elaborates the DOM as a current compact representation of visual features.

A. Discrete Orthogonal Polynomials

The set of polynomials that are orthogonal on the uniform lattice $\{u = 0, 1, 2, \dots, N - 1\}$, Tchebichef, Krawtchouk, and Hahn polynomials, are discussed in this subsection.

The discrete orthogonal polynomials $p_n(u)$ are defined as the polynomial solutions of the following difference equation

$$\sigma(u)\Delta\nabla p_n(u) + \tau(u)\Delta p_n(u) + \lambda_n p_n(u) = 0, \quad (1)$$

where $\Delta p_n(u) = p_n(u + 1) - p_n(u)$ and $\nabla p_n(u) = p_n(u) - p_n(u - 1)$ denote the forward and backward first-order difference operators, respectively. $\sigma(u)$ and $\tau(u)$ are the functions of the second and first degree, respectively. λ_n is an appropriate constant (see [22] for more details). The set of polynomials $\{p_n(u)\}$ with weight $w(u)$ and norm ρ_n satisfies an orthogonality condition

$$\sum_{u=0}^s p_n(u)p_m(u)w(u) = \rho(n)\delta_{nm}, \quad 0 \leq n, m \leq s, \quad (2)$$

where s is $N - 1$ for discrete Tchebichef, Hahn polynomials and N for Krawtchouk polynomials, and δ_{mn} denotes the Dirac function. Subsequently, the normalized discrete orthogonal polynomials can be obtained by appropriate weighting

$$\tilde{p}_n(u) = p_n(u) \sqrt{\frac{w(u)}{\rho(n)}}. \quad (3)$$

Hence, the orthogonality condition in (2) can be re-expressed as

$$\sum_{u=0}^s \tilde{p}_n(u)\tilde{p}_m(u) = \delta_{nm}, \quad 0 \leq n, m \leq s. \quad (4)$$

The computation of normalized polynomials $\tilde{p}_n(u)$ is elaborated below.

B. Computation of Normalized Discrete Orthogonal Polynomials

The computation of normalized polynomials $\tilde{p}_n(u)$ has consistently been a major concern [23]–[25]. The numerical instability can therefore easily occur in the evaluation of such polynomials if the recurrence relations are not properly used. The u recurrence relation is more advantageous than n recurrence relation in avoiding error accumulation in the result [26]. Hence, the following will introduce the recurrence relations with respect to u for these three polynomials: the normalized Tchebichef, Krawtchouk, and Hahn polynomials.

According to (1) and (3), the recurrence relations with respect to u can be expressed as

$$\tilde{p}_n(u) = \frac{1}{\sigma(u-1) + \tau(u-1)} \left((2\sigma(u-1) + \tau(u-1) - \lambda_n) \sqrt{\frac{w(u)}{w(u-1)}} \tilde{p}_n(u-1) - \sigma(u-1) \sqrt{\frac{w(u)}{w(u-2)}} \tilde{p}_n(u-2) \right). \quad (5)$$

Referring to [27], we present some information that facilitates the computation of (5) in Table I for normalized Tchebichef, Krawtchouk, and Hahn polynomials. And the initial values of the normalized polynomials, $\tilde{p}_n(0)$ and $\tilde{p}_n(1)$, are listed in Table II.

TABLE I
COMPUTATIONAL INFORMATION FOR THE NORMALIZED TCHEBICHEF $\tilde{t}_n(u; N)$, KRAWTCHOUK $\tilde{k}_n(u; p, N)$ AND HAHN $\tilde{h}_n(u; a, b, N)$ POLYNOMIALS, ($p \in (0, 1)$ FOR KRAWTCHOUK, AND $a, b \in \mathbb{N}$ FOR HAHN).

$\tilde{p}_n(u)$	$\tilde{t}_n(u; N)$	$\tilde{k}_n(u; p, N)$	$\tilde{h}_n(u; a, b, N)$
$\sigma(u)$	$u(N - u)$	u	$u(N + a - u)$
$\tau(u)$	$N - 1 - 2x$	$\frac{Np-u}{1-p}$	$(b+1)(N-1) - (a+b+2)u$
λ_n	$n(n+1)$	$\frac{n}{1-p}$	$n(a+b+n+1)$
$\frac{w(u)}{w(u-1)}$	1	$\frac{p}{1-p} \frac{N-u+1}{u}$	$\frac{b+u}{u} \frac{N-u}{N+a-u}$
$\frac{w(u)}{w(u-2)}$	1	$\frac{p^2}{(1-p)^2} \frac{(N-u+1)(N-u+2)}{(u-1)u}$	$\frac{(b+u-1)(b+u)}{(u-1)u} \frac{(N-u)(N-u+1)}{(N-u+a)(N-u+a+1)}$

TABLE II
INITIAL VALUES OF THE RECURRENCE RELATION WITH RESPECT TO u FOR THE NORMALIZED TCHEBICHEF, KRAWTCHOUK, AND HAHN POLYNOMIALS, ($p \in (0, 1)$ FOR KRAWTCHOUK AND $a, b \in \mathbb{N}$ FOR HAHN).

$\tilde{p}_n(u)$	$u = 0$	$u = 1$
$\tilde{t}_n(u; N)$	$-\sqrt{\frac{N-n}{N+n}} \sqrt{\frac{2n+1}{2n-1}} \tilde{t}_{n-1}(0; N),$ $\tilde{t}_0(0; N) = \sqrt{\frac{1}{N}}$	$\left(1 - \frac{n(n+1)}{N-1}\right) \tilde{t}_n(0; N)$
$\tilde{k}_n(u; p, N)$	$-\sqrt{\frac{N-n+1}{n}} \sqrt{\frac{p}{1-p}} \tilde{k}_{n-1}(0; p, N),$ $\tilde{k}_0(0; p, N) = (1-p)^{N/2}$	$\left(1 - \frac{n}{Np}\right) \sqrt{\frac{w(1)}{w(0)}} \tilde{k}_n(0; p, N)$
$\tilde{h}_n(u; a, b, N)$	$-\sqrt{\frac{(N-n)(n+b)(a+b+n)}{(a+n)(a+b+n+N)n}} \sqrt{\frac{a+b+2n+1}{a+b+2n-1}} \tilde{h}_{n-1}(0; a, b, N),$ $\tilde{h}_0(0; a, b, N) = \sqrt{\prod_{i=1}^{b+1} \frac{a+i}{N+a+i-1}}$	$\left(1 - \frac{n(n+a+b+1)}{(b+1)(N-1)}\right) \sqrt{\frac{w(1)}{w(0)}} \tilde{h}_n(0; a, b, N)$

C. Relationship among Normalized Tchebichef, Krawtchouk and Hahn polynomials

It is noted that the normalized Tchebichef, Krawtchouk, and Hahn polynomials are interrelated [26]. If we define $p = b/(a+b)$ and $t = a+b$, then the parameters in normalized Hahn polynomial can be expressed as

$$\begin{cases} b = pt \\ a = (1-p)t. \end{cases} \quad (6)$$

If $t \rightarrow 0$ or $t \rightarrow \infty$, the normalized Hahn polynomial is converted to normalized Tchebichef polynomial ($a = 0, b = 0$) or Krawtchouk polynomial ($a+b \rightarrow \infty$), respectively [28]

$$\begin{aligned} \lim_{t \rightarrow 0} \tilde{h}_n(u; a, b, N) &= \tilde{t}_n(u; N), \\ \lim_{t \rightarrow \infty} \tilde{h}_n(u; a, b, N) &= \tilde{k}_n(u; p, N). \end{aligned} \quad (7)$$

Fig. 1 shows plots of the normalized polynomials ($N = 512$, $n = 0, 1, \dots, 5$). It can be observed from Figs. 1a and 1d that for $a = 0, b = 0$, the normalized Hahn polynomial is equivalent to the normalized Tchebichef polynomial. Moreover, the normalized Tchebichef polynomial satisfies the symmetry property

$$\tilde{t}_n(N-1-u; N) = (-1)^n \tilde{t}_n(u; N), \quad (8)$$

which can be exploited to significantly reduce the time required for computation. It can be shown that, if $t \gg 2N$ ($t = 20N$), we can confirm that the normalized Hahn polynomial satisfactorily approximates the normalized Krawtchouk polynomial (see Figs. 1b, 1c, 1e and 1f). The parameter of the normalized Krawtchouk polynomial $p \in (0, 1)$ is used to shift the region-of-interest (ROI). If $p < 0.5$, the ROI is on the left

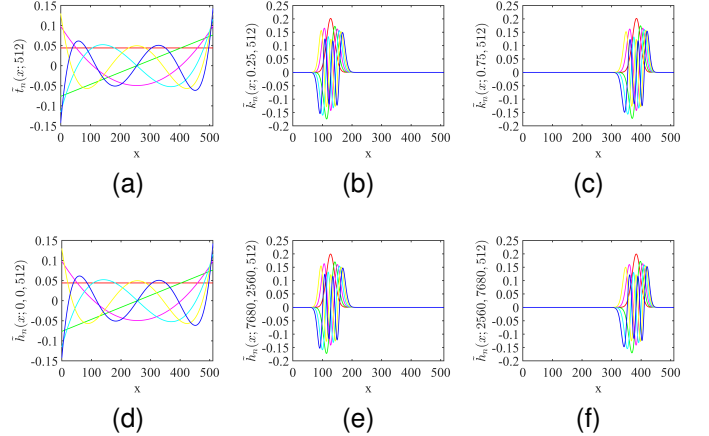


Fig. 1. Plots of normalized polynomials ($N = 512$, $n = 0, 1, \dots, 5$). (a) Tchebichef polynomials. (b) Krawtchouk polynomials ($p = 0.25$). (c) Krawtchouk polynomials ($p = 0.75$). (d) Hahn polynomials ($a = 0, b = 0$). (e) Hahn polynomials ($a = 7680, b = 2560$). (f) Hahn polynomials ($a = 2560, b = 7680$).

(see Fig. 1b), whilst the ROI is on the right if $p > 0.5$ (see Fig. 1c). The specific quantitative description is discussed in Section III-A. From Fig. 1, it can be seen that the normalized Tchebichef polynomial holds the global information extraction capability, the normalized Krawtchouk polynomial holds the local information extraction capability, and the normalized Hahn polynomial holds both of these capabilities. Hence, the latter is more suitable as a visual feature, whose verification will be presented in Section V.

D. DOM

This subsection discusses DOM as novel compact visual features, which are derived from normalized polynomials $\tilde{p}_n(u)$.

Given a digital image $\mathbf{I}(u, v)$ with size $N \times M$, that is, $u \in [0, N - 1]$ and $v \in [0, M - 1]$, the $(n + m)$ th order moments with a variable normalized orthogonal polynomials as basis function for an image is defined as

$$P_{nm} = \sum_u \sum_v \mathbf{p}_{nm}(u, v) \mathbf{I}(u, v), \quad n, m = 0, 1, \dots, s, \quad (9)$$

where orthogonal operators $\mathbf{p}_{nm}(u, v) = \tilde{p}_n(u) \tilde{p}_m(v)$. Hence, TM, KM and HM can be written as

$$T_{nm} = \sum_u \sum_v \mathbf{t}_{nm}(u, v) \mathbf{I}(u, v), \quad (10)$$

$$K_{nm}(\alpha p, \beta p) = \sum_u \sum_v \mathbf{k}_{nm}(u, v, \alpha p, \beta p) \mathbf{I}(u, v), \quad (11)$$

$$H_{nm}(\alpha a, \alpha b, \beta a, \beta b) = \sum_u \sum_v \mathbf{h}_{nm}(u, v, \alpha a, \alpha b, \beta a, \beta b) \mathbf{I}(u, v), \quad (12)$$

where TM, KM and HM operators can be defined as

$$\begin{aligned} \mathbf{t}_{nm}(u, v) &= \tilde{t}_n(u; N) \tilde{t}_m(v; M), \\ \mathbf{k}_{nm}(u, v, \alpha p, \beta p) &= \tilde{k}_n(u; \alpha p, N) \tilde{k}_m(v; \beta p, M), \\ \mathbf{h}_{nm}(u, v, \alpha a, \alpha b, \beta a, \beta b) &= \tilde{h}_n(u; \alpha a, \alpha b, N) \tilde{h}_m(v; \beta a, \beta b, M). \end{aligned}$$

DOM have been widely adopted for image compression and filtering in the image processing domain [23], [24], [26], such that they achieve better image dimensionality reduction and robustness when used as image features in DVS. If we choose the order of orthogonal moments to be l , the VS features can be represented as

$$\mathbf{s} = [P_{00}, P_{10}, P_{01}, \dots, P_{nm}]^T, \quad n + m \leq l, \quad (13)$$

where P_{nm} can be calculated from (9). Hence, we propose three VS schemes, namely: TM-based VS (TM-VS), KM-based VS (KM-VS) and HM-based VS (HM-VS). If we perform KM-VS or HM-VS, the parameters $\alpha p, \beta p$ in (11) and $\alpha a, \alpha b, \beta a, \beta b$ in (12) need to be determined. And the order of orthogonal moments l also needs to be calculated. The following describes how to derive these parameters.

III. ADAPTIVE PARAMETER SELECTION

Articles [24] and [26] show that suitable parameters can effectively reduce the error of reconstructing images by KM and HM. This is because appropriate parameters can capture useful information about the image. Inspired by, adaptive parameter selection is extremely critical for VS. In a VS phase, the current image $\mathbf{I}(u, v)$ and the desired image $\mathbf{I}^*(u, v)$ are known. Therefore, this section will present the method for adaptive selection of parameters $\alpha p, \beta p, \alpha a, \alpha b, \beta a, \beta b$, and l based on $\mathbf{I}(u, v)$ and $\mathbf{I}^*(u, v)$.

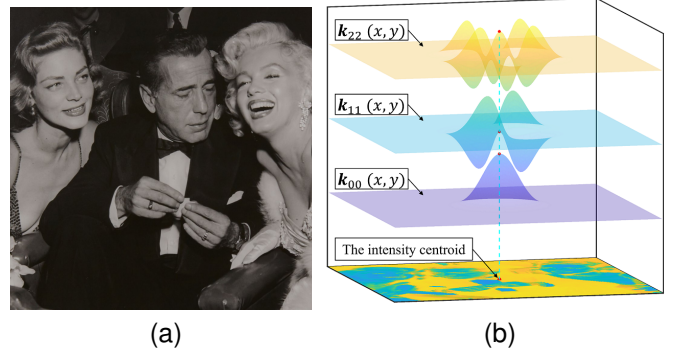


Fig. 2. An example of the calculation of the Krawtchouk moment parameters ($N = M = 128$). (a) The example image (assuming the initial image is the same as the desired image). (b) Surface plots of the 0th, 2nd, and 4th order Krawtchouk moment operators ($\alpha p = 0.5074$ and $\beta p = 0.4812$).

A. Selection of KM Parameters αp and βp

This subsection describes the adaptive KM parameters selection method. We first define a superposition projection of an image in the u and v directions, respectively. They can be written as

$$\alpha \mathbf{I}(u) = \sum_v \mathbf{I}(u, v), \quad \beta \mathbf{I}(v) = \sum_u \mathbf{I}(u, v). \quad (14)$$

Then the intensity centroid (u_c, v_c) of the image is calculated by

$$u_c = \frac{\sum_u u \alpha \mathbf{I}(u)}{\sum_u \alpha \mathbf{I}(u)}, \quad v_c = \frac{\sum_v v \beta \mathbf{I}(v)}{\sum_v \beta \mathbf{I}(v)}. \quad (15)$$

Note that this is equivalent to the calculation using geometric moments [7]. Similarly, the intensity centroid (u_c^*, v_c^*) of the desired image can also be obtained from $\mathbf{I}^*(u, v)$. Therefore, the intensity centroid of two images as a whole is defined as

$$\bar{u}_c = \frac{u_c + u_c^*}{2}, \quad \bar{v}_c = \frac{v_c + v_c^*}{2}. \quad (16)$$

We can use the weighting functions $\alpha w_K(u)$ and $\beta w_K(v)$ to represent the importance of the KM on the u and v directions of the image, respectively, which are defined as

$$\begin{aligned} \alpha w_K(u; \alpha p, N) &= \binom{N}{u} (\alpha p)^u (1 - \alpha p)^{N-u}, \\ \beta w_K(v; \beta p, M) &= \binom{M}{v} (\beta p)^v (1 - \beta p)^{M-v}. \end{aligned} \quad (17)$$

They are the probability mass function (PMF) of a binomial distribution. So the mean of weighting functions are

$$\alpha \mu_K = \alpha p N, \quad \beta \mu_K = \beta p M. \quad (18)$$

We set $\bar{u}_c = \alpha \mu_K$ and $\bar{v}_c = \beta \mu_K$, then αp and βp can be calculated by

$$\alpha p = \frac{\bar{u}_c}{N}, \quad \beta p = \frac{\bar{v}_c}{M}. \quad (19)$$

Fig. 2 shows an example of the calculation of the KM parameters. Assuming that the same initial and desired images as in Fig. 2a, the intensity centroid of the image is $u_c = 64.9448$ and $v_c = 61.5981$. Hence, KM parameters are $\alpha p = 0.5074$ and $\beta p = 0.4812$. Fig. 2b shows the surface plots of the 0th,

2nd, and 4th order KM operators (\mathbf{k}_{00} , \mathbf{k}_{11} , and \mathbf{k}_{22}). The ROI of the KM is only a part of the whole image, so some information is lost.

In summary, ${}^\alpha p$ and ${}^\beta p$ affect the position of the ROI in the u and v directions during the VS, respectively, but the range of the ROI cannot be changed.

B. Selection of HM Parameters ${}^\alpha a$, ${}^\alpha b$, ${}^\beta a$ and ${}^\beta b$

This subsection describes how to adaptively select the HM parameters. This method is inspired by [26].

First, injecting (19) in (6), we can obtain

$$\begin{cases} {}^\alpha b(\mathbf{I}) = \frac{\bar{u}_c}{N} {}^\alpha \bar{t}(\mathbf{I}) \\ {}^\alpha a(\mathbf{I}) = (1 - \frac{\bar{u}_c}{N}) {}^\alpha \bar{t}(\mathbf{I}), \end{cases} \quad \begin{cases} {}^\beta b(\mathbf{I}) = \frac{\bar{v}_c}{M} {}^\beta \bar{t}(\mathbf{I}) \\ {}^\beta a(\mathbf{I}) = (1 - \frac{\bar{v}_c}{M}) {}^\beta \bar{t}(\mathbf{I}). \end{cases} \quad (20)$$

Then we only need to determine the parameters, ${}^\alpha \bar{t}(\mathbf{I})$, ${}^\beta \bar{t}(\mathbf{I}) \in [0, \infty)$, which are related to the dispersion of VS image. The dispersion are defined as ${}^\alpha \bar{d}(\mathbf{I}) \in [0, N-1]$ and ${}^\beta \bar{d}(\mathbf{I}) \in [0, M-1]$. And we can let

$${}^\alpha \bar{t}(\mathbf{I}) = e^{{}^\alpha \kappa {}^\alpha \bar{d}(\mathbf{I}) + {}^\alpha \varrho}, \quad {}^\beta \bar{t}(\mathbf{I}) = e^{{}^\beta \kappa {}^\beta \bar{d}(\mathbf{I}) + {}^\beta \varrho}, \quad (21)$$

where

$${}^\alpha \bar{d}(\mathbf{I}) = \frac{{}^\alpha d(\mathbf{I}) + {}^\alpha d^*(\mathbf{I})}{2}, \quad {}^\beta \bar{d}(\mathbf{I}) = \frac{{}^\beta d(\mathbf{I}) + {}^\beta d^*(\mathbf{I})}{2},$$

where ${}^\alpha d(\mathbf{I})$, ${}^\beta d(\mathbf{I})$, ${}^\alpha d^*(\mathbf{I})$ and ${}^\beta d^*(\mathbf{I})$ denote the dispersion of the initial and desired image in the u and v directions, respectively. The following will introduce how to calculate these parameters ${}^\alpha \kappa$, ${}^\alpha \varrho$, ${}^\alpha d(\mathbf{I})$, ${}^\alpha d^*(\mathbf{I})$, ${}^\beta \kappa$, ${}^\beta \varrho$, ${}^\beta d(\mathbf{I})$ and ${}^\beta d^*(\mathbf{I})$.

While the weighting function (17) of Krawtchouk polynomials is the PMF of a binomial distribution, the mean is $\mu = Np$ and variance is $\sigma^2 = Np(1-p)$. According to (6), if $t \rightarrow \infty$, the weighting function of the Hahn polynomial is equivalent to the weighting function of the Krawtchouk polynomial. Thus, it is reasonable to assume that if $t \rightarrow \infty$, the variance of the weighting function of the Hahn polynomial is also $\sigma^2 = Np(1-p)$.

So far, we can use the following constraints:

- if ${}^\alpha d(\mathbf{I}) = 3{}^\alpha \sigma = 3\sqrt{\bar{u}_c(1 - \bar{u}_c/N)}$, ${}^\alpha t(\mathbf{I}) = \infty \approx 20N$;
- if ${}^\alpha d(\mathbf{I}) = N-1$, ${}^\alpha t(\mathbf{I}) = 0 \approx 0.01$;
- if ${}^\beta d(\mathbf{I}) = 3{}^\beta \sigma = 3\sqrt{\bar{v}_c(1 - \bar{v}_c/M)}$, ${}^\beta t(\mathbf{I}) = \infty \approx 20M$;
- if ${}^\beta d(\mathbf{I}) = M-1$, ${}^\beta t(\mathbf{I}) = 0 \approx 0.01$.

The matrix for this constraint is expressed as

$$\mathbf{B}\boldsymbol{\chi} = \mathbf{C}, \quad (22)$$

where

$$\mathbf{B} = \begin{bmatrix} 3\sqrt{\bar{u}_c(1 - \bar{u}_c/N)} & 1 & 0 & 0 \\ N-1 & 1 & 0 & 0 \\ 0 & 0 & 3\sqrt{\bar{v}_c(1 - \bar{v}_c/M)} & 1 \\ 0 & 0 & M-1 & 1 \end{bmatrix},$$

$$\boldsymbol{\chi} = \begin{bmatrix} {}^\alpha \kappa & {}^\alpha \varrho & {}^\beta \kappa & {}^\beta \varrho \end{bmatrix}^T,$$

$$\mathbf{C} = \begin{bmatrix} \ln 20N & \ln 0.01 & \ln 20M & \ln 0.01 \end{bmatrix}^T.$$

It is easy to get $\boldsymbol{\chi} = \mathbf{B}^{-1}\mathbf{C}$. Finally, we only need to calculate the ${}^\alpha d(\mathbf{I})$ and ${}^\beta d(\mathbf{I})$ of the image in VS to obtain ${}^\alpha t(\mathbf{I})$ and ${}^\beta t(\mathbf{I})$.

It is well known that the PMF of a binomial distribution approximates the probability density function (PDF) of a Gaussian distribution when $Np, N(1-p) > 5$ [26]. 3σ rule can be expressed as $P_{3\sigma} = \Pr(\mu - 3\sigma \leq u \leq \mu + 3\sigma) \approx 0.9974$ for the Gaussian distribution, where $\Pr(\cdot)$ is the probability function. When $Np, N(1-p) > 5$ and $t \rightarrow \infty$, the weighting function of the Hahn polynomial is the Gaussian-like distribution, whose 3σ rule can be expressed as $P_{3\sigma}^h \approx P_{3\sigma} \approx 0.9974$. The PMFs of the image with respect to u and v are

$${}^\alpha \mathbf{P}(u) = \frac{{}^\alpha \mathbf{I}(u)}{\sum_u {}^\alpha \mathbf{I}(u)}, \quad {}^\beta \mathbf{P}(v) = \frac{{}^\beta \mathbf{I}(v)}{\sum_v {}^\beta \mathbf{I}(v)}, \quad (23)$$

where ${}^\alpha \mathbf{I}(u)$ and ${}^\beta \mathbf{I}(v)$ are defined by (14). Then we can calculate ${}^\alpha d(\mathbf{I})$ and ${}^\beta d(\mathbf{I})$ as

$$\begin{aligned} {}^\alpha d(\mathbf{I}) &= \arg_d {}^\alpha \mathbf{P}(\bar{u}_c) \\ &+ \sum_{i=1}^d {}^\alpha \mathbf{P}(\bar{u}_c + i) + {}^\alpha \mathbf{P}(\bar{u}_c - i) \geq P_{3\sigma}^h, \\ {}^\beta d(\mathbf{I}) &= \arg_d {}^\beta \mathbf{P}(\bar{v}_c) \\ &+ \sum_{j=1}^d {}^\beta \mathbf{P}(\bar{v}_c + j) + {}^\beta \mathbf{P}(\bar{v}_c - j) \geq P_{3\sigma}^h. \end{aligned} \quad (24)$$

Note that we specify that if $u < 0$ or $u > N-1$, ${}^\alpha P(u) = 0$; if $v < 0$ or $v > M-1$, ${}^\beta P(v) = 0$. Similarly, ${}^\alpha d^*(\mathbf{I})$ and ${}^\beta d^*(\mathbf{I})$ can also be determined. So far, the necessary parameters for calculating ${}^\alpha \bar{t}(\mathbf{I})$ and ${}^\beta \bar{t}(\mathbf{I})$ have been determined. And we can calculate them according to (21). Finally, (20) can be used to obtain the HM parameters ${}^\alpha a$, ${}^\alpha b$, ${}^\beta a$ and ${}^\beta b$. It can be seen that the above method uses the 3σ rule. When the image noise is large, the 2σ rule is also used to calculate these parameters.

Fig. 3 shows an example of the calculation of the HM parameters. Still assuming that the initial and desired images are the same as Fig. 2a, the HM parameters obtained by calculation is ${}^\alpha a = 5$, ${}^\alpha b = 6$, ${}^\beta a = 7$ and ${}^\beta b = 6$. And surface plots of the 0th, 2nd, and 4th order HM operators (\mathbf{h}_{00} , \mathbf{h}_{11} , and \mathbf{h}_{22}) are showed in Fig. 3a, whose ROI is significantly larger than the ROI of KM operators in Fig. 2b. The images in Fig. 2a are scaled and translated for better illustrate the adaptability of the method proposed in this subsection. The HM parameters calculated from the transformed image are ${}^\alpha a = 175$, ${}^\alpha b = 127$, ${}^\beta a = 198$ and ${}^\beta b = 136$. And surface plots are showed in Fig. 3b. As a comparison, Fig. 4 shows surface plots of the 0th, 2nd, and 4th order TM operators (\mathbf{t}_{00} , \mathbf{t}_{11} , and \mathbf{t}_{22}). Because Tchebichef polynomials do not have any parameters to be adjusted, the TM operators are the same for both the original image and the transformed image. It is clear that the adaptive HM operators have excellent performance for both the original image and the transformed images, which is not the case for the KM and TM operators.

In short, $b/(a+b)$ and $a+b$ affect the position and range of the ROI during the VS, thus HM-VS can take into account

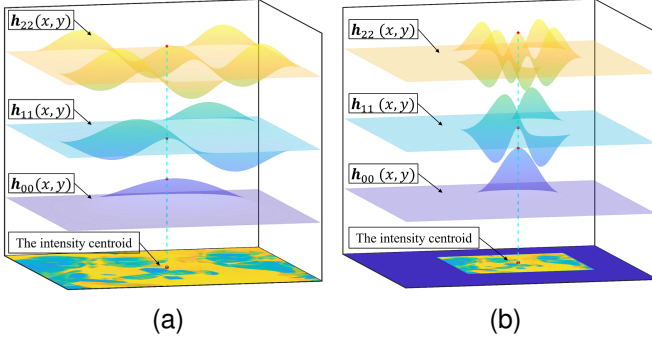


Fig. 3. An example of the calculation of the Hahn moment parameters ($N = M = 128$). (a) Surface plots of the 0th, 2nd, and 4th order Hahn moment operators for the origin image ($\alpha a = 5, \alpha b = 6, \beta a = 7$ and $\beta b = 6$). (b) Surface plots of the 0th, 2nd, and 4th order Hahn moment operators for the transformed image ($\alpha a = 175, \alpha b = 127, \beta a = 198$ and $\beta b = 136$).

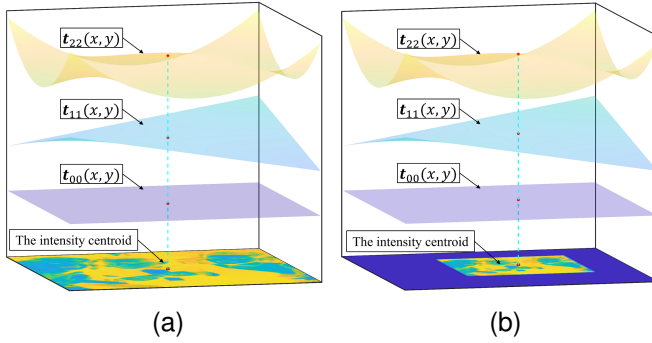


Fig. 4. Surface plots of the 0th, 2nd, and 4th order Tchebichef moment operators ($N = M = 128$). (a) The calculation result of the original image. (b) The calculation result of the transformed image.

both global and local information of the image through flexible parameter tuning.

C. Selection of DOM Order l

If the order of the orthogonal moments is determined, then the VS features can be obtained according to (13). When the order of the orthogonal moments is small, the VS feature mainly considers the coarse information of the image, which has the advantage of better image filtering and compression properties. However, since it does not take into account the detailed information of the image, this makes the VS procedure prone to local minima. In contrast, when the order of the orthogonal moments is large, the VS features mainly consider the detailed information of the image, which has the advantage of great convergence accuracy. However, the VS process converges slowly due to its excessive attention to detailed information. The following introduces a method for selecting the orthogonal moments order l to exploit their advantages while avoiding their shortcomings.

We intend to approach the target object quickly with a small order when it is far from the target pose, and converge with high accuracy with a large order when it is close to the target pose. First we define the minimum and maximum orders (l_{\min}

and l_{\max}), which are empirically fixed values. The required order can then be expressed as

$$l = (l_{\max} - l_{\min})\eta + l_{\min}, \quad \eta \in [0, 1], \quad l \in \mathbb{N}, \quad (25)$$

where η is defined as

$$\eta = \frac{\bar{e}_{I^o}}{\bar{e}_{I^o} + \lambda_{\eta} \bar{e}_I}, \quad (26)$$

where \bar{e}_I and \bar{e}_{I^o} are the mean square error of the current and initial images, respectively, and are defined as

$$\bar{e}_I = \frac{\sum_u \sum_v (\mathbf{I}(u, v) - \mathbf{I}^*(u, v))^2}{N \times M},$$

$$\bar{e}_{I^o} = \frac{\sum_u \sum_v (\mathbf{I}^o(u, v) - \mathbf{I}^*(u, v))^2}{N \times M},$$

where $\mathbf{I}^o(u, v)$, $\mathbf{I}(u, v)$ and $\mathbf{I}^*(u, v)$ are the initial, current and desired images, respectively. Based on the control law of exponentially decreasing feature error introduced in Section IV, it is reasonable to assume that the \bar{e}_I also decreases exponentially, i.e. $\bar{e}_I = \bar{e}_{I^o} e^{-\lambda_{\eta} t}$. Hence, (26) can be rewritten as

$$\eta = \frac{1}{1 + \lambda_{\eta} e^{-\lambda_{\eta} t}},$$

where η is the sigmoid function with an "S"-shaped curve, which is exactly what we need. In the following, we describe how to calculate λ_{η} in (26).

We normally consider VS convergence when $\bar{e}_I = \epsilon$ is satisfied, where ϵ is a fixed value and $\bar{e}_{I^o} \gg \epsilon$. λ_{η} is designed as a linear function of \bar{e}_I . Therefore, we can use the following constraints:

- if $\bar{e}_I = \bar{e}_{I^o}$, $\lambda_{\eta} = \bar{e}_{I^o} / \epsilon$;
- if $\bar{e}_I = \epsilon$, $\lambda_{\eta} = 0$.

For the former, we have $\eta = \frac{1}{1 + \bar{e}_{I^o} / \epsilon} \approx 0, l = l_{\min}$; for the latter, we have $\eta = 1, l = l_{\max}$. Based on the above constraints, λ_{η} can be calculated as

$$\lambda_{\eta} = \frac{\bar{e}_{I^o}}{\epsilon(\bar{e}_{I^o} - \epsilon)}(\bar{e}_I - \epsilon). \quad (27)$$

Injecting (27) in (26), η can be expressed as

$$\eta = \frac{1}{1 + \frac{\bar{e}_I}{\epsilon} \frac{\bar{e}_{I^o} - \epsilon}{\bar{e}_{I^o} - \epsilon}}. \quad (28)$$

So far, l can be calculated by (25). More details about the choice of the l_{\min} and l_{\max} are discussed in Section V-F.

Take $l = 4$ as an example, Fig. 5 shows the VS loss landscape of the error function on an x/y translation motion around the desired pose. The methods of TM-VS (see Fig. 5b) and HM-VS (see Fig. 5d) have better convergence domain than DVS (see Fig. 5a). And the HM-VS loss landscape is the most satisfactory. However, the convergence domain of KM-VS (see Fig. 5c) is the worst. This is mainly due to the fact that the ROI of the KM operators is not the whole image (see Fig. 2b), and the large translations around the desired pose in this experiment resulted in parts of the image being out of field-of-view. In addition, if $l = N + M - 2$, the visual features are the set of all DOM $\mathbf{s} = [P_{00}, P_{10}, P_{01}, \dots, P_{N-1, M-1}]^T$. Hence, the TM-VS and HM-VS schemes proposed in this study are equivalent as the DVS [11], [18].

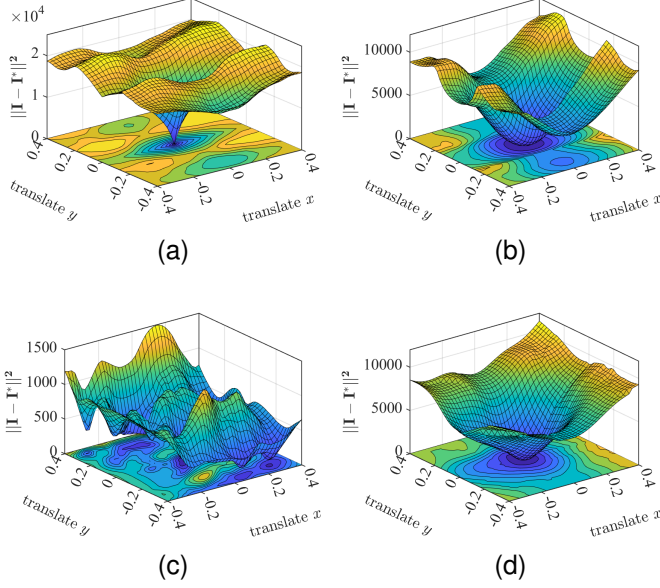


Fig. 5. The VS loss landscape on an x/y translation motion around the desired pose. (a) DVS. (b) TM-VS. (c) KM-VS. (d) HM-VS

IV. INTERACTION MATRIX OF DOM

The aim of VS is to minimize the feature error $\mathbf{e}(t)$, which is typically defined by

$$\mathbf{e}(t) = \mathbf{s} - \mathbf{s}^*, \quad (29)$$

where \mathbf{s}^* is the desired value of visual features \mathbf{s} to be reached in the image [29]. The key of VS is the interaction matrix \mathbf{L}_e that links the time variation of feature error to the camera velocity \mathbf{v} [17]

$$\dot{\mathbf{e}} = \dot{\mathbf{s}} - \dot{\mathbf{s}}^* = \mathbf{L}_e \mathbf{v}. \quad (30)$$

To ensure an exponential decoupled decrease of the feature error [29], the control law is designed as

$$\mathbf{v} = -\lambda \hat{\mathbf{L}}_e^\dagger (\mathbf{s} - \mathbf{s}^*), \quad (31)$$

where λ is a positive scalar, $\hat{\mathbf{L}}_e$ is an estimation or an approximation of \mathbf{L}_e and $(\cdot)^\dagger$ is the Moore-Penrose pseudo-inverse. The following will describe how to calculate $\hat{\mathbf{L}}_e$.

Based on (13), the visual features \mathbf{s} and \mathbf{s}^* can be written as

$$\begin{aligned} \mathbf{s} &= P_{nm} = \sum_u \sum_v \mathbf{p}_{nm}(u, v) \mathbf{I}(u, v), \\ \mathbf{s}^* &= P_{nm}^* = \sum_u \sum_v \mathbf{p}_{nm}(u, v) \mathbf{I}^*(u, v). \end{aligned} \quad (32)$$

The time variation of visual features in (32) can be calculated as

$$\begin{aligned} \dot{\mathbf{s}} &= \sum_u \sum_v \left(\mathbf{p}_{nm}(u, v) \dot{\mathbf{I}}(u, v) + \dot{\mathbf{p}}_{nm}(u, v) \mathbf{I}(u, v) \right), \\ \dot{\mathbf{s}}^* &= \sum_u \sum_v \dot{\mathbf{p}}_{nm}(u, v) \mathbf{I}^*(u, v). \end{aligned} \quad (33)$$

Hence, (30) can be expressed as

$$\dot{\mathbf{e}} = \sum_u \sum_v \left(\mathbf{p}_{nm}(u, v) \dot{\mathbf{I}}(u, v) + \dot{\mathbf{p}}_{nm}(u, v) (\mathbf{I}(u, v) - \mathbf{I}^*(u, v)) \right). \quad (34)$$

A. Interaction Matrix of TM

This subsection describes how to calculate the interaction matrix of TM. It is clear from Section II-D that the TM operators are not time-varying ($\dot{\mathbf{t}}_{nm} = 0$). So (34) can be simplified as

$$\dot{\mathbf{e}} = \sum_u \sum_v \mathbf{p}_{nm}(u, v) \dot{\mathbf{I}}(u, v). \quad (35)$$

We introduce the calculation of $\dot{\mathbf{I}}$. The basic hypothesis assumes the temporal constancy of the brightness for a physical point between two successive images. This hypothesis leads to the so-called optical flow constraint equation that links the temporal variation of the luminance I to the image motion at pixel point $\mathbf{u} = (u, v)$: [10], [11]

$$\nabla I^T \dot{\mathbf{u}} + \dot{I} = 0, \quad (36)$$

where $\nabla I^T = [\nabla I_u, \nabla I_v]$ is the spatial gradient at the pixel point \mathbf{u} , where ∇I_u and ∇I_v are the components along u and v of the image gradient. Further, the relationship linking the time variation in the coordinates of a pixel point in the image with the camera velocity is

$$\dot{\mathbf{u}} = \mathbf{L}_u \mathbf{v}, \quad (37)$$

where

$$\begin{aligned} \mathbf{L}_u &= \mathbf{L}_\kappa \mathbf{L}_x \\ &= \begin{bmatrix} \kappa_u & 0 \\ 0 & \kappa_v \end{bmatrix} \begin{bmatrix} -\frac{1}{Z} & 0 & \frac{x}{Z} & xy & -(1+x^2) & y \\ 0 & -\frac{1}{Z} & \frac{y}{Z} & 1+y^2 & -xy & -x \end{bmatrix} \end{aligned}$$

where κ_u and κ_v are the horizontal and vertical scale factors of the camera intrinsic matrix, and \mathbf{L}_x is the interaction matrix related to a image point $\mathbf{x} = (x, y)$ [29]. According to (36) and (37), we can obtain that

$$\dot{I} = \mathbf{L}_I \mathbf{v}, \quad (38)$$

where

$$\mathbf{L}_I = -\nabla I^T \mathbf{L}_u.$$

By plugging (38) into (35), the time variation of the feature error becomes

$$\dot{\mathbf{e}} = \mathbf{L}_e \mathbf{v}, \quad (39)$$

where the interaction matrix with respect to \mathbf{e} is

$$\mathbf{L}_e = \sum_u \sum_v \mathbf{p}_{nm}(u, v) \mathbf{L}_I.$$

Finally, the $\hat{\mathbf{L}}_e$ can be designed as

$$\begin{aligned} \hat{\mathbf{L}}_e &= \frac{1}{2} (\mathbf{L}_e + \mathbf{L}_e^*) \\ &= \sum_u \sum_v \mathbf{p}_{nm}(u, v) \frac{\mathbf{L}_I + \mathbf{L}_I^*}{2}, \end{aligned} \quad (40)$$

since it was shown to be efficient for very large camera displacements [30].

B. Interaction Matrix of KM and HM

This subsection describes how the KM and HM interaction matrices are calculated. Both the KM and HM operators are time-varying ($\dot{\mathbf{k}}_{nm} \neq 0, \dot{\mathbf{h}}_{nm} \neq 0$). Hence, $\dot{\mathbf{p}}_{nm}(u, v)$ in (34) needs to be calculated. In the remainder of the paper, we will omit the subscript nm and the arguments (u, v) for the sake of clarity.

Following Sections III-A and III-B, the KM and HM parameters are adjusted to ensure that the ROI of the operator varies with the image. Therefore, it is reasonable to formulate hypothesis that the temporal constancy of the KM and HM operators. Based on (16), we see that the rate of change of the operators \mathbf{p} is half that of the image \mathbf{I} . We can get that

$$p(\mathbf{u}, t) = p(\mathbf{u} + \frac{\Delta \mathbf{u}}{2}, t + \Delta t). \quad (41)$$

A first-order Taylor development of (41) gives

$$\frac{1}{2} \nabla p^T \dot{\mathbf{u}} + \dot{p} = 0, \quad (42)$$

where $\nabla p^T = [\nabla p_u, \nabla p_v]$ is the spatial gradient of the operators p and \dot{p} is its time derivation. So \dot{p} can be expressed as

$$\dot{p} = -\frac{1}{2} (\nabla p_u \dot{u} + \nabla p_v \dot{v}). \quad (43)$$

By plugging (43) into (34), the time variation of the feature error becomes

$$\begin{aligned} \dot{\mathbf{e}} &= \sum_u \sum_v \left(\mathbf{p} \dot{\mathbf{I}} - \frac{1}{2} (\nabla \mathbf{p}_u \dot{u} + \nabla \mathbf{p}_v \dot{v}) (\mathbf{I} - \mathbf{I}^*) \right) \\ &= \sum_u \sum_v \left(\mathbf{p} \dot{\mathbf{I}} - \frac{1}{2} (\nabla \mathbf{p}_u \mathbf{I} \dot{u} + \nabla \mathbf{p}_v \mathbf{I} \dot{v}) \right. \\ &\quad \left. + \frac{1}{2} (\nabla \mathbf{p}_u \mathbf{I}^* \dot{u} + \nabla \mathbf{p}_v \mathbf{I}^* \dot{v}) \right). \end{aligned} \quad (44)$$

The Green's theorem can be expressed as

$$\sum_u \sum_v \left(\frac{\partial Q}{\partial u} - \frac{\partial P}{\partial v} \right) = \sum_{\partial u} P + \sum_{\partial v} Q. \quad (45)$$

We define $Q = pI$ and $P = 0$, then

$$\frac{\partial Q}{\partial u} = \nabla p_u I + p \nabla I_u, \quad \frac{\partial P}{\partial v} = 0. \quad (46)$$

Substituting (46) in (45), we get

$$\sum_u \sum_v \nabla p_u I = \sum_{\partial v} pI - \sum_u \sum_v p \nabla I_u \quad (47)$$

It is reasonable to assume that the pI lying on the border are all zero (see Figs. 2 and 3). Then the term $\sum_{\partial v} pI$ in (47) is equal to zero. We, therefore, can obtain

$$\begin{aligned} \sum_u \sum_v \nabla p_u I &= - \sum_u \sum_v p \nabla I_u, \\ \sum_u \sum_v \nabla p_u I^* &= - \sum_u \sum_v p \nabla I_u^*. \end{aligned} \quad (48)$$

Similarly, if we define $Q = 0$ and $P = pI$, then we can get

$$\begin{aligned} \sum_u \sum_v \nabla p_v I &= - \sum_u \sum_v p \nabla I_v, \\ \sum_u \sum_v \nabla p_v I^* &= - \sum_u \sum_v p \nabla I_v^*. \end{aligned} \quad (49)$$

By plugging (48) and 49 into (44), we obtain

$$\begin{aligned} \dot{\mathbf{e}} &= \sum_u \sum_v \left(\mathbf{p} \dot{\mathbf{I}} + \frac{1}{2} (\mathbf{p} \nabla I_u \dot{u} + \mathbf{p} \nabla I_v \dot{v}) \right. \\ &\quad \left. - \frac{1}{2} (\mathbf{p} \nabla I_u^* \dot{u} + \mathbf{p} \nabla I_v^* \dot{v}) \right). \end{aligned} \quad (50)$$

Based on (36), (50) can be simplified as

$$\begin{aligned} \dot{\mathbf{e}} &= \sum_u \sum_v \left(\mathbf{p} \dot{\mathbf{I}} - \frac{1}{2} \mathbf{p} \dot{\mathbf{I}} + \frac{1}{2} \mathbf{p} \dot{\mathbf{I}}^* \right) \\ &= \sum_u \sum_v \mathbf{p} \frac{\dot{\mathbf{I}} + \dot{\mathbf{I}}^*}{2} = \mathbf{L}_e \mathbf{v}, \end{aligned} \quad (51)$$

where the interaction matrix with respect to \mathbf{e} is

$$\hat{\mathbf{L}}_e = \sum_u \sum_v \mathbf{p} \frac{\mathbf{L}_I + \mathbf{L}_I^*}{2} \quad (52)$$

It is important to note that the (40) and (52) are the same, so the interaction matrix for HM, KM and HM has the same form.

V. EXPERIMENTAL RESULTS

In this section, we evaluate the proposed control scheme by combining simulation and experimental results. Since the generic framework to consider DOM as a visual feature is proposed for the first time, the VS schemes (TM-VS, KM-VS and HM-VS) are simply compared with each other in Section V-A. Then, Section V-B presents results for challenging experiments highlighting the contribution of using DOM as visual features. In Section V-C, we investigate the robustness of the proposed VS scheme when some noise is added to the images. The HM-VS scheme is compared with three state-of-the-art approaches in Section V-D. Section V-E shows experiments conducted with a robot in the real environments. Finally, the minimum and maximum orders (l_{\min} and l_{\max}) are discussed in Section V-F.

A. VS in Classical Simulation Environments

Simulation results were first performed for comparison between TM-VS, KM-VS and HM-VS. Given a vision sensor and a target object as examples, the co-simulation was performed on the MATLAB 2021b and CoppeliaSim 4.2 platforms. In the following simulations, the image size is 512×512 , and the minimum and maximum orders are $l_{\min} = 4$ and $l_{\max} = 8$, respectively.

Experiment #1 (see Fig. 6): This experiment has been carried out using a classic scene and controlling 6-DoF. Figs. 6a and 6b show the initial and desired images, respectively. The error between the initial and desired pose is given by $(0.48\text{m}, -0.26\text{m}, -0.37\text{m}, -4.54^\circ, -17.06^\circ, -30.37^\circ)$. Since the visual features computed by the TM, KM, and HM are different from each other, we compare the convergence of the three schemes by pixel errors $\|\mathbf{I} - \mathbf{I}^*\|^2$, and the results are shown in Fig. 6c. With respect to TM-VS and KM-VS, HM-VS have a faster convergence rate (213 iterations vs. 235 and 225). Although we cannot control the trajectory of the camera in Cartesian space, it is clear from Fig. 6d that the trajectory

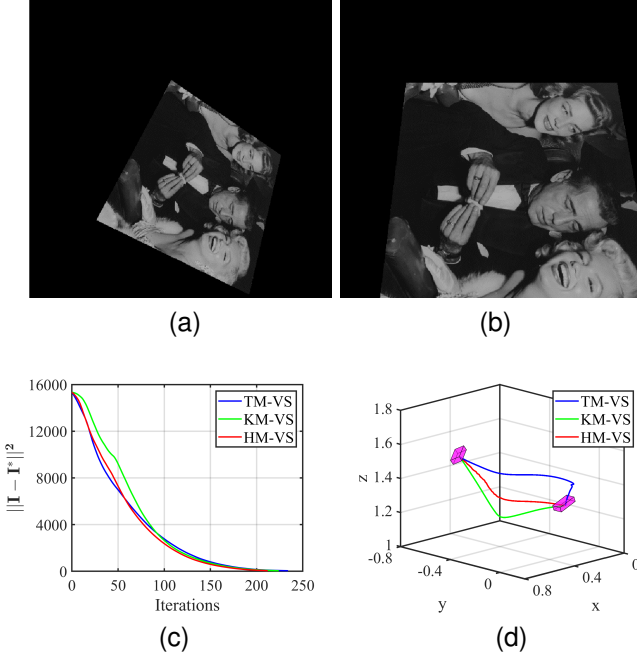


Fig. 6. Experiment #1: Comparison between TM-VS, KM-VS and HM-VS in a classic scene. (a) Initial image. (b) Desired image. (c) The pixel errors. (d) The camera trajectories (in m).

of HM-VS is better than those of TM-VS and KM-VS. The control results for each method are analyzed below.

Figs. 7, 8 and 9 show the results for TM-VS, KM-VS and HM-VS, respectively. The exponentially decreasing feature errors validate the control law we designed in Section IV (see Figs. 7a, 8a and 9a). The perturbation of the velocity plots (see Figs. 7b, 8b and 9b) is due to the nonlinearity and discontinuity of the cost function, as well as to the changes in the image caused by appearance and disappearance of portions of the scene from the camera field-of-view. Nevertheless, these VS schemes have successfully converged to the desired pose. The order of the DOM during VS shown in Figs. 7c, 8c, and 9c follows the same trend as we expected in Section III-C. The "S"-shaped curve completes the trade-off between convergence rate and accuracy. In the KM-VS scheme, the parameters α_p and β_p of the KM are calculated online using the method proposed in Section III-A to ensure successful control (see Fig. 8d). Similarly, the parameters α_a , α_b , β_a and β_b of HM are calculated online using the approach proposed in Section III-B to properly adjust the ROI in the HM-VS scheme (see Fig. 9d).

In summary, the proposed TH-VS, KM-VS, and HM-VS schemes are all effective for the classical scenario.

B. VS in Complex 2-D and 3-D Simulation Environments

Experiment #2 (see Fig. 10): The scenario with a complex textured plane and control of 6-DoF was used for this experiment. In addition, the textured plane is partially outside the camera field-of-view in the desired image (see Figs. 6a and 6b). The large displacement between the initial and desired pose is given by $(0.70\text{m}, -0.03\text{m}, -0.74\text{m}, 7.85^\circ, -14.07^\circ,$

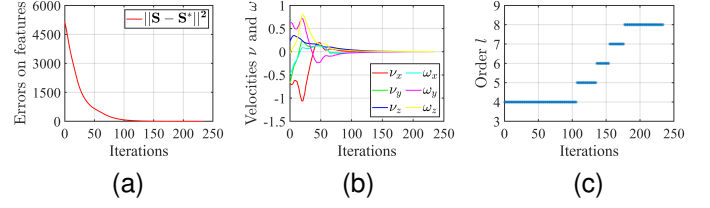


Fig. 7. Results for TM-VS in Experiment #1. (a) Errors on features. (b) Camera velocities (in m/s and rad/s). (c) Order of DOM as visual features.

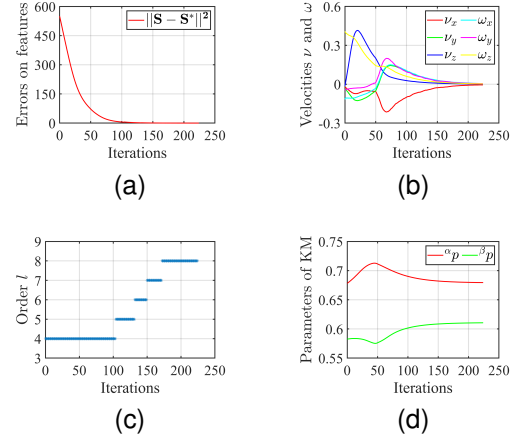


Fig. 8. Results for KM-VS in Experiment #1. (a) Errors on features. (b) Camera velocities (in m/s and rad/s). (c) Order of DOM as visual features. (d) The parameters of KM.

-41.61°). The pixel errors and camera trajectories for the TM-VS, KM-VS, and HM-VS methods are shown in Figs. 10c and 10d, respectively. Only HM-VS has been successful in this task. For TM-VS, it ultimately fails because the textured plane is all outside the camera field-of-view. For KM-VS, it fails in that it ends up in a local minimum, which is consistent with the fact that there are a number of local minima in the VS loss landscape represented in Fig. 5c. The details of HM-VS are illustrated in Fig. 11. The non-exponential decrease in

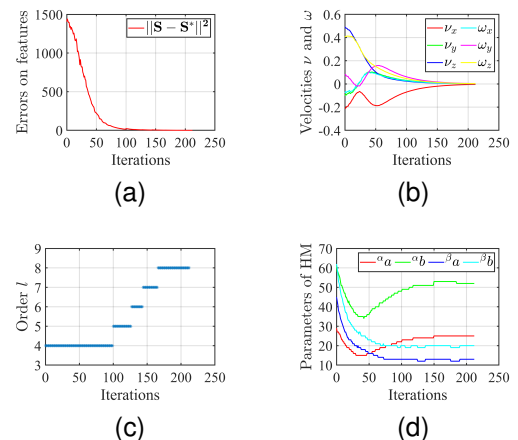


Fig. 9. Results for HM-VS in Experiment #1. (a) Errors on features. (b) Camera velocities (in m/s and rad/s). (c) Order of DOM as visual features. (d) The parameters of HM.

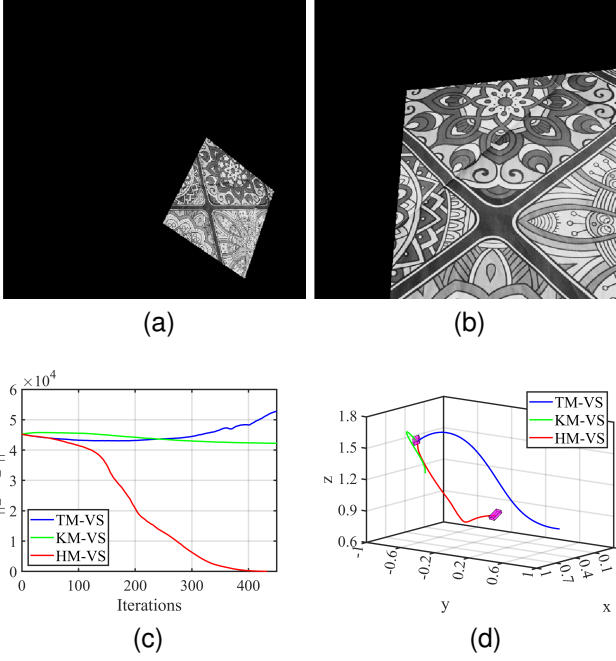


Fig. 10. Experiment #2: Comparison between TM-VS, KM-VS and HM-VS in a complex 2-D scene. (a) Initial image. (b) Desired image. (c) The pixel errors. (d) The camera trajectories (in m).

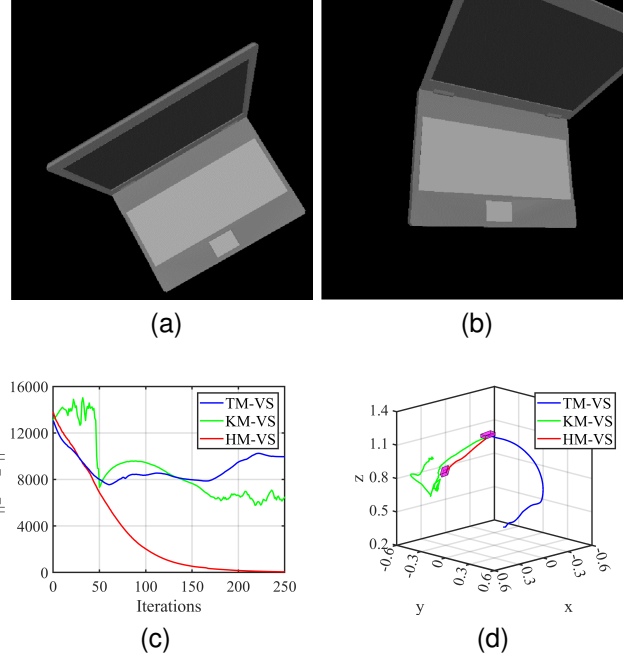


Fig. 12. Experiment #3: Comparison between TM-VS, KM-VS and HM-VS in a 3-D virtual environment. (a) Initial image. (b) Desired image. (c) The pixel errors. (d) The camera trajectories (in m).

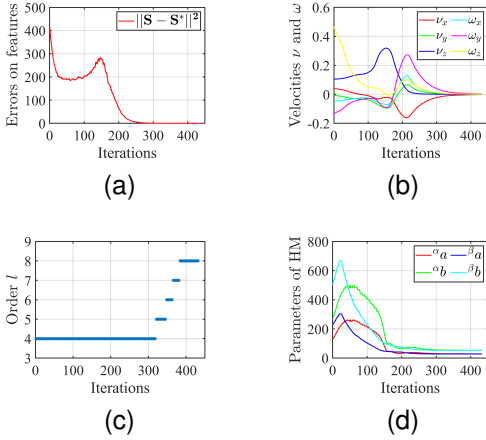


Fig. 11. Results for HM-VS in Experiment #2. (a) Errors on features. (b) Camera velocities (in m/s and rad/s). (c) Order of DOM as visual features. (d) The parameters of HM.

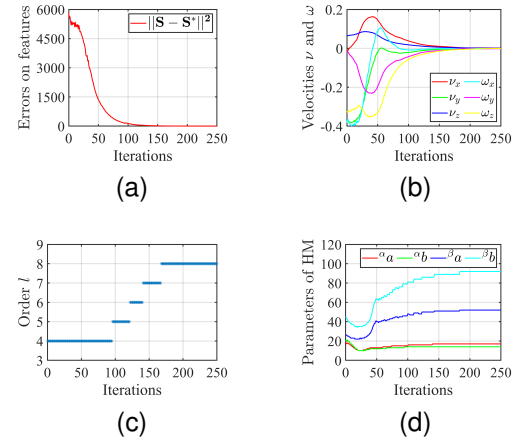


Fig. 13. Results for HM-VS in Experiment #3. (a) Errors on features. (b) Camera velocities (in m/s and rad/s). (c) Order of DOM as visual features. (d) The parameters of HM.

feature error is caused by a little part of the textured plane going out of the field-of-view during VS (see Fig. 11a). It is for the above reasons that the low-order components of the "S"-shaped curve account for the main part (see Fig. 11c).

Experiment #3 (see Fig. 12): In this experiment, we compare the proposed VS schemes in a 3-D virtual environment. Taking the "laptop" as an example, the initial and desired images are shown in Figs. 12a and 12b, respectively. The "laptop" is partially outside the camera field-of-view in the desired image. Figs. 12c and 12d illustrate the pixel errors and camera trajectories obtained from the TM-VS, KM-VS and HM-VS methods. The displacement between the desired and the initial camera poses is $(-0.41\text{m}, -0.26\text{m}, -0.06\text{m},$

$15.41^\circ, 22.63^\circ, 35.13^\circ)$. The orientations around the two axes orthogonal to the optical axis of the camera is of interest. Only the HM-VS approach converges perfectly to the desired pose with a final pose error equal to $(0.5\text{mm}, 0.5\text{mm}, 0.5\text{mm}, 0.02^\circ, 0.02^\circ, 0.02^\circ)$. Both TM-VS and KM-VS fail in that they both end up in a local minimum. The details of HM-VS are shown in Fig. 13. The exponentially decreasing feature errors (see Fig. 13a), "S"-shaped curve (see Fig. 13c), and real-time adjustment of HM parameters (see Fig. 13d) validate the effectiveness of HM-VS for 3D environments.

In conclusion, the HM-VS scheme is significantly better than the TM-VS and KM-VS schemes due to its flexible parameter tuning mechanism.

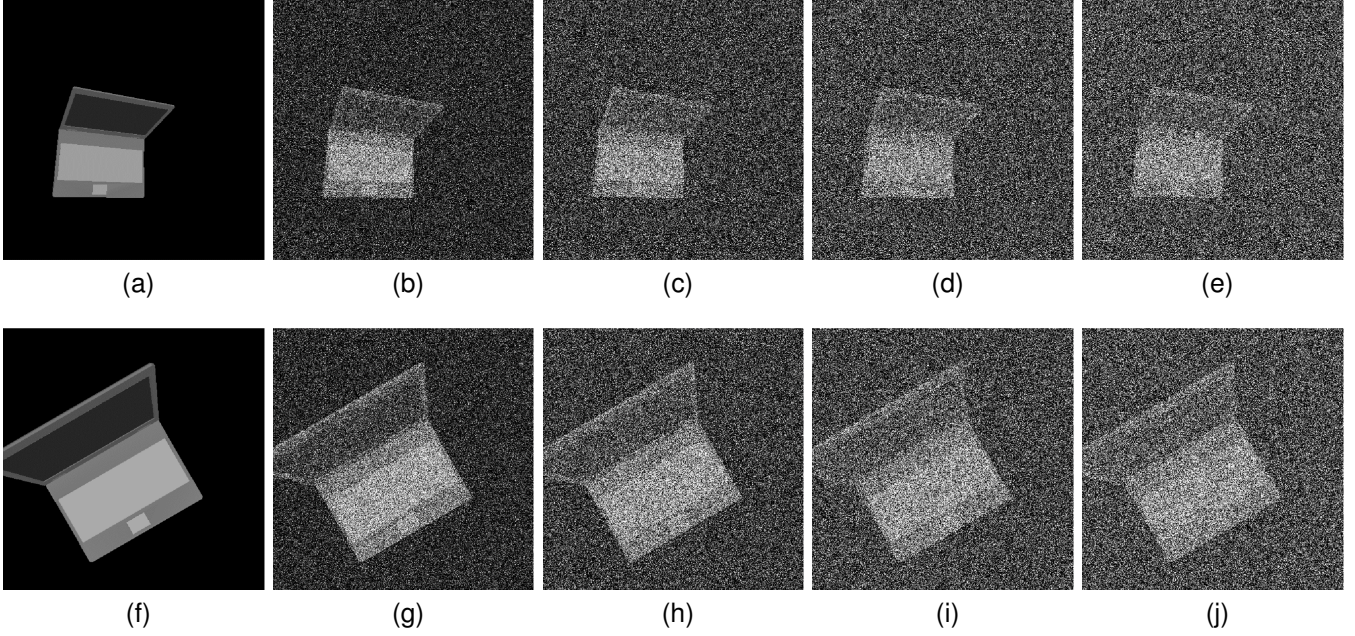


Fig. 14. Experiment #4: Gaussian noise robustness evaluation. (a)-(e) Initial images with variance $\sigma^2 = 0, 0.2, 0.4, 0.6$ and 0.8 , respectively. (f)-(j) Desired images with variance $\sigma^2 = 0, 0.2, 0.4, 0.6$ and 0.8 , respectively.

C. Evaluation of the Robustness with respect to Noise

Experiment #4 (see Fig. 14): The robustness of the proposed TM-VS, KM-VS, and HM-VS schemes was compared in this subsection. We let $l = 8$ during the VS process. Fig. 14 exhibits an experiment evaluating the noise robustness. The displacement between the desired and the initial camera poses remains the same for each experiment: $(0.23\text{m}, -0.39\text{m}, -0.29\text{m}, -21.59^\circ, -19.39^\circ, -33.19^\circ)$. First, the VS is performed without any image noise $\sigma^2 = 0$ (see Figs. 14a and 14f). Next, a stepwise increasing Gaussian noise is added to the initial image and the desired image (see Figs. 14b-14e and 14g-14j). Specifically, the intensity of the noise is enhanced between each experiment with a variance $\sigma^2 = 0.2, 0.4, 0.6$ and 0.8 . The average convergence error (position and orientation) are shown in Table III.

From Table III, it can be easily seen that both TM-VS and HM-VS are particularly robust against image noise. KM-VS is only available for $\sigma^2 = 0$ in this experiment. The accuracy at convergence decreases as the noise intensity increases, but it is still excellent for the added excessive noise, thanks to the filtering properties of the DOM. In addition, the HM-VS scheme has advantages over other methods.

D. Comparisons with Three State-of-the-Art Approaches

In this section, simulations are performed to evaluate the proposed HM-VS scheme while allowing a fair comparison of the three state-of-the-art methods: DVS [11], DCT-VS [18], and PGM-VS [17]. Both HM-VS and DCT-VS methods use the method proposed in Section III-C to determine the order. The minimum and maximum orders are still $l_{\min} = 4, l_{\max} = 8$. The required parameter λ_{gi} in the PGM-VS is determined to be $\lambda_{gi} = 10$ or $\lambda_{gi} = 16$. To ensure the same conditions,

TABLE III
RESULTS OF THE AVERAGE CONVERGENCE ERROR (POSITION AND ORIENTATION) OBTAINED BY TM-VS, KM-VS AND HM-VS METHODS.

	TM-VS	KM-VS	HM-VS
$\sigma^2 = 0$	0.05mm, 0.01°	9.28mm, 0.37°	0.03mm, 0.00°
$\sigma^2 = 0.2$	2.20mm, 0.24°	N/A	0.99mm, 0.20°
$\sigma^2 = 0.4$	7.80mm, 0.67°	N/A	3.68mm, 0.22°
$\sigma^2 = 0.6$	13.30mm, 1.10°	N/A	4.09mm, 0.58°
$\sigma^2 = 0.8$	32.28mm, 2.29°	N/A	12.10mm, 0.97°

all methods are based on the Gauss-Newton algorithm. The image size is 128×128 in the following simulations.

Case #1 (see Fig. 15): In the case of a large displacement facing a 2-D scene, the noise-free initial and desired images are shown in Figs. 15a and 15b, respectively. Fig. 15c illustrates the obtained camera trajectories using these methods in the absence of Gaussian noise $\sigma^2 = 0$, where only PGM-VS ($\lambda_{gi} = 16$) is a failure. For the convergence rate, HM-VS (137 iterations) is more satisfactory than DVS (1590 iterations), DCT-VS (148 iterations), and PGM-VS ($\lambda_{gi} = 10$) (192 iterations). Fig. 15d shows the obtained camera trajectories using these methods in the presence of Gaussian noise $\sigma^2 = 0.6$, where only DCT-VS and HM-VS are able to perform the task. However, the final error of HM-VS (43.4mm, 2.6mm, 5.5mm, 0.2°, 2.7°, 1.3°) is better than that of DCT-VS (171.7mm, 2.4mm, 63.7mm, 0.8°, 12.1°, 1.9°).

Case #2 (see Fig. 16): A challenging case where a large part of the desired image is absent in the initial image is presented in Fig. 16. Fig. 16c illustrates the camera trajectories obtained using these methods in the absence of Gaussian noise $\sigma^2 = 0$, of which only HM-VS and DVS methods can successfully

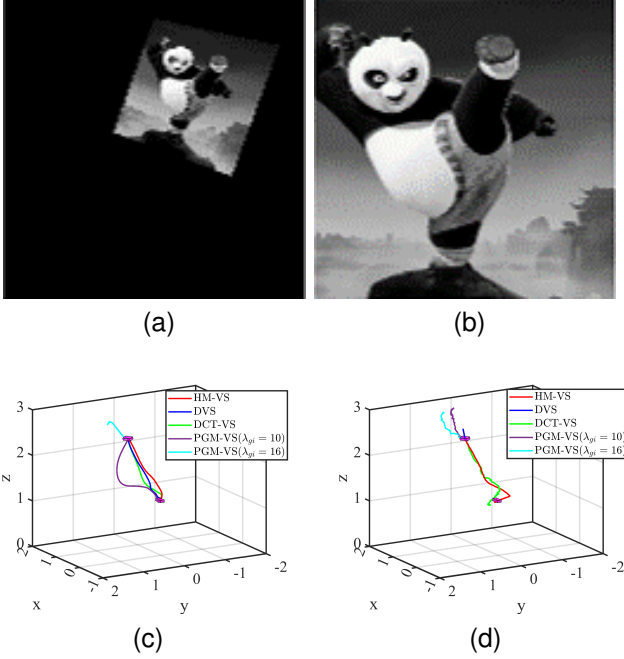


Fig. 15. Case #1: An example with classical scene, and camera trajectories. (a) Initial image. (b) Desired image. (c) The camera trajectories with Gaussian noise $\sigma^2 = 0$ (in m). (d) The camera trajectories with Gaussian noise $\sigma^2 = 0.6$ (in m).

drive the camera to the desired pose. When adding a Gaussian noise $\sigma^2 = 0.2$ on both the desired and the current images, only the HM-VS approach succeeds, all other methods fail because they fall into local minima or are out of field-of-view.

Case #3 (see Fig. 17): In the case of a large displacement facing a 3-D scene, the noise-free initial and desired images are shown in Figs. 17a and 17b, respectively. When Gaussian noise is absent, the HM-VS and DVS methods can successfully drive the camera to the desired pose (see Fig. 17c). When Gaussian noise $\sigma^2 = 0.5$ is present, only HM-VS, PGM-VS ($\lambda_{gi} = 10$), and PGM-VS ($\lambda_{gi} = 16$) methods cause the camera to converge next to the desired pose, but the final visual alignment of these methods is negligible (see Fig. 17d).

Table IV provides the successful and failed convergences for these cases. Only the HM-VS method is available for all cases. The experiments show that the robustness of the DVS method is not satisfactory, as it does not have the ability to filter. Strictly speaking, DCT-VS is also a DOM-based VS method, but HM-VS has more advantages due to its flexible parameter tuning mechanism. Finally, the PGM-VS method does not perform as well as the HM-VS method in all these cases, an essential reason being the poor choice of the parameter λ_{gi} .

E. Experimental Results on a 7-DoF Robot

The aim of this subsection is to demonstrate that the proposed method works well even in real environments for both 2-D and 3-D objects. The experiments were conducted on a 7-DoF Franka Emika robotic arm equipped with an Intel RealSense L515 LiDAR camera. The LiDAR camera simultaneously acquires color and depth images, with a (640×480) resolution. The camera calibration as well as the hand-eye

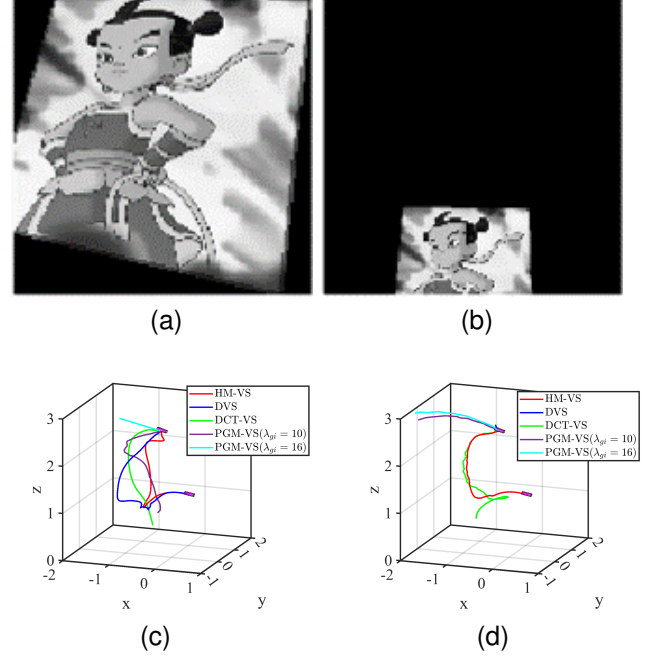


Fig. 16. Case #2: An example with large difference between initial and desired images, and camera trajectories. (a) Initial image. (b) Desired image. (c) The camera trajectories with Gaussian noise $\sigma^2 = 0$ (in m). (d) The camera trajectories with Gaussian noise $\sigma^2 = 0.2$ (in m).

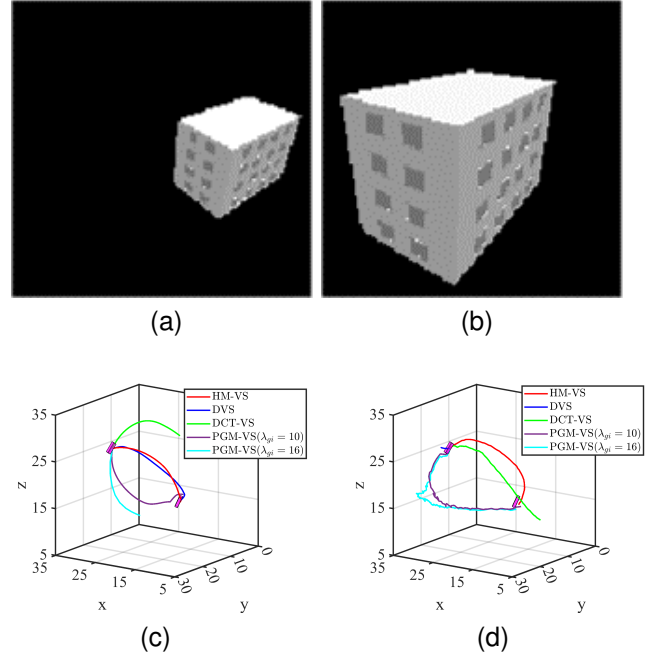


Fig. 17. Case #3: An example with a large displacement 3-D scene, and camera trajectories. (a) Initial image. (b) Desired image. (c) The camera trajectories with Gaussian noise $\sigma^2 = 0$ (in m). (d) The camera trajectories with Gaussian noise $\sigma^2 = 0.5$ (in m).

TABLE IV
HM-VS, DVS, DCT-VS, AND PGM-VS METHODS COMPARISON.

	Case #1		Case #2		Case #3	
	Noiseless	Noise	Noiseless	Noise	Noiseless	Noise
HM-VS	✓	✓	✓	✓	✓	✓
DVS	✓	○	✓	○	✓	○
DCT-VS	✓	✓	○	○	✗	✗
PGM-VS($\lambda_{gi} = 10$)	✓	✗	○	✗	○	✓
PGM-VS($\lambda_{gi} = 16$)	✗	✗	✗	✗	○	✓

Successful (✓) and failed (✗) convergences for the three cases (see Figs. 15-17). A blue marker (○) means that the camera has converged next to the desired pose and that the final visual alignment is not negligible.

calibration have been done in an offline step. The depths are not estimated but available from the camera truth data. The image processing and the control law computation are performed on a PC equipped with a 14-cores 2.3 GHz Intel Core i7-12700H. This allows a frequency for the servo loop around 2 Hz. The required parameters are $l_{\min} = 6$ and $l_{\max} = 16$ in the following experiences.

Experiment #5 (see Figs. 18 and 19): Fig. 18 illustrates the 2-D real experimental environment. The scene contains a 2-D object under common lighting conditions. Figs. 19a and 19b show the initial and desired images, respectively, where complex plane is partially outside the camera field-of-view in the desired image. The displacement between the initial and the desired camera poses is given by $(0.15\text{m}, -0.13\text{m}, -0.09\text{m}, -8.68^\circ, -1.13^\circ, -3.00^\circ)$. All three methods, TM-VS, KM-VS, and HM-VS, are used to perform VS control. The camera trajectories obtained from these methods are presented in Fig. 19d. Both TM-VS and HM-VS schemes can converge the pose error to less than $(2\text{mm}, 2\text{mm}, 2\text{mm}, 0.5^\circ, 0.5^\circ, 0.5^\circ)$. Unfortunately, the KM-VS scheme fails with the present case. The pixel errors $\|\mathbf{I} - \mathbf{I}^*\|^2$ obtained from these three methods are shown in Fig. 19c. Specifically, the TM-VS and HM-VS require 118 and 90 iterations, respectively. The HM-VS scheme still has the fastest convergence rate. The control results of the TM-VS and HM-VS methods are illustrated in Figs. 20 and 21, respectively. It is worth explaining that the variation of the HM parameter in Fig. 21d is much smaller than in the simulations, since the background is not black in the real experiment, making the ROI of the current and desired images less variable.

This experiment demonstrates that the proposed method is still valid despite VS in a 2D real environment.

Experiment #6 (see Figs. 22 and 23): The experiment is implemented in a 3-D real environment. A realistic scenario is set up by placing a number of 3-D objects of varying shapes, sizes, and colors in the scene as shown in Fig. 22. The desired image is given in Fig. 23b while the initial one is given in Fig. 23a. The challenge of this experiment is that some objects are outside the camera field-of-view in the desired image. The corresponding displacement is $(0.04\text{m}, 0.13\text{m}, -0.31\text{m}, 20.88^\circ, -3.76^\circ, -17.70^\circ)$. The pixel errors $\|\mathbf{I} - \mathbf{I}^*\|^2$ and the camera trajectories obtained from these three methods (TM-VS, KM-VS, and HM-VS) are shown in Figs. 23c and

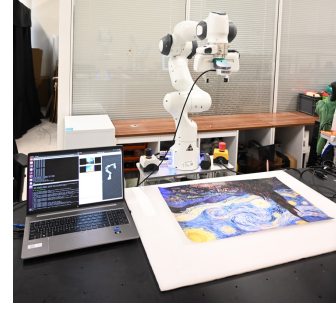


Fig. 18. The real 2-D experimental environment.

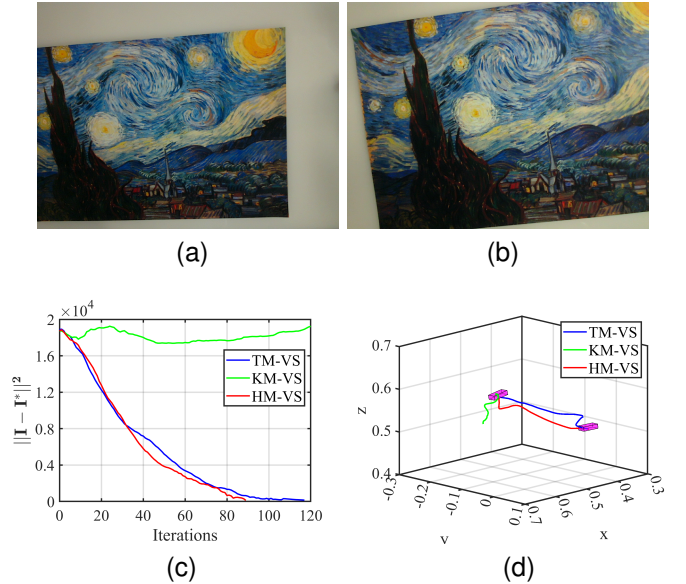


Fig. 19. Experiment #5: Comparison between TM-VS, KM-VS and HM-VS in a 2-D real environment. (a) Initial image. (b) Desired image. (c) The pixel errors. (d) The camera trajectories (in m).

23d, respectively. It can be easily seen that only the KM-VS and HM-VS methods succeed in the VS task, while the TM-VS approach fails because it falls into local minima in the VS. Both KM-VS and HM-VS schemes can converge the pose error to less than $(1\text{mm}, 1\text{mm}, 1\text{mm}, 0.3^\circ, 0.3^\circ, 0.3^\circ)$. However, the convergence rate of the HM-VS method is better than that of KM-VS. The details of the KM-VS and HM-VS

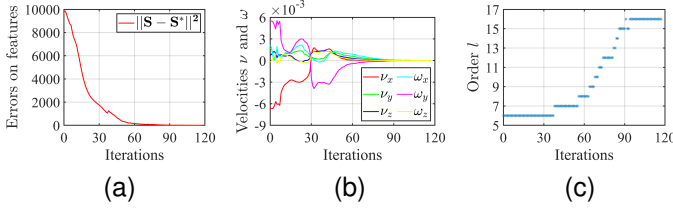


Fig. 20. Results for TM-VS in Experiment #5. (a) Errors on features. (b) Camera velocities (in m/s and rad/s). (c) Order of DOM as visual features.

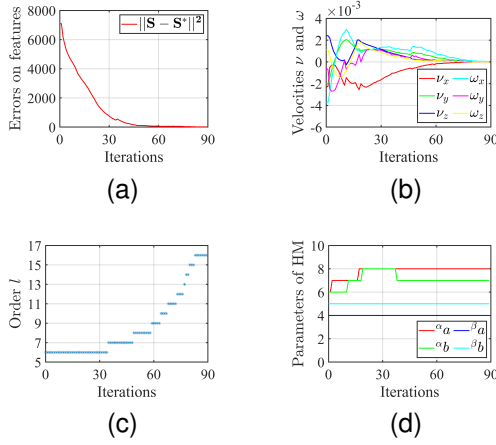


Fig. 21. Results for HM-VS in Experiment #5. (a) Errors on features. (b) Camera velocities (in m/s and rad/s). (c) Order of DOM as visual features. (d) The parameters of HM.

methods are illustrated in Figs. 24 and 25, respectively.

Overall, convergence and stability are still achieved despite VS in a 3-D real environment, which validates the efficacy of our method.

F. Discussion

The previous experiments have demonstrated the effectiveness of our method even in complex environments. However, as explained in Section III-C, two parameters are involved in our approach: the minimum order of DOM (l_{\min}) and the maximum order of DOM (l_{\max}). In general, the choice of these parameters depends on the convergence rate, the convergence error, and many other factors, which is still an open question. This section, therefore, discusses qualitatively the effect of the DOM order on the VS.

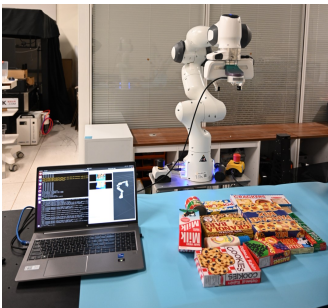


Fig. 22. The real 3-D experimental environment.



Fig. 23. Experiment #6: Comparison between TM-VS, KM-VS and HM-VS in a 3-D real environment. (a) Initial image. (b) Desired image. (c) The pixel errors. (d) The camera trajectories (in m).

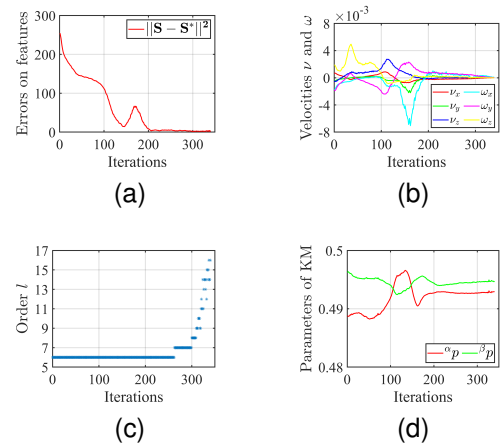


Fig. 24. Results for KM-VS in Experiment #6. (a) Errors on features. (b) Camera velocities (in m/s and rad/s). (c) Order of DOM as visual features. (d) The parameters of KM.

We add a Gaussian noise $\sigma^2 = 0.4$ to the image and then perform the HM-VS with $l = 3, 6, 9, 12, 15$, respectively. The results are presented in Fig. 26. The initial and desired images are shown in Figs. 26a and 26b, respectively. It is clear from Fig. 26e that HM-VS can perform the task with different values of l . The simple relationship between the DOM order, the convergence rate and the convergence error can be obtained from the position and orientation errors (see 26c and 26d):

- for the convergence rate, the smaller the DOM order, the faster the convergence;
- for convergence errors, the higher the order, the better the accuracy.

In addition, we found that VS can fail due to falling into local minima when the order l is too large.

We may therefore give the following advice for the choice

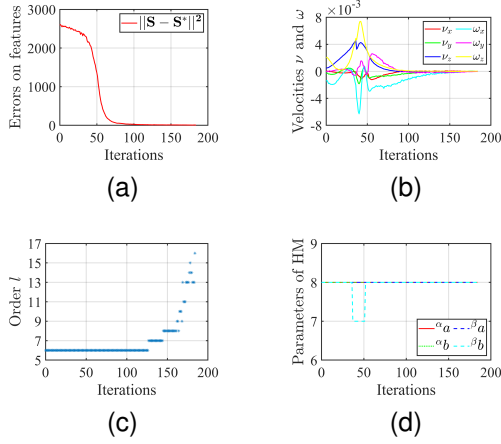


Fig. 25. Results for HM-VS in Experiment #6. (a) Errors on features. (b) Camera velocities (in m/s and rad/s). (c) Order of DOM as visual features. (d) The parameters of HM.

of l_{\min} and l_{\max} :

- l_{\min} should be as small as possible in the case of convergence;
- l_{\max} should be as large as possible in the case of a suitable convergence rate.

VI. CONCLUSION

In this paper, for the first time we proposed a generic framework to consider DOM as visual features for DVS. Moreover, it was shown that the interaction matrix related to DOM can be calculated explicitly. Taking TM, KM, and HM as examples, three DVS schemes, TM-VS, KM-VS, and HM-VS, are proposed, and adaptive estimation methods for the associated parameters are also introduced. The experimental results indicated that our proposed control schemes are effective and robust for VS of both 2-D and 3-D objects. This is due to the image compression and filtering properties of the DOM. Note that the HM-VS method outperforms state-of-the-art methods in terms of convergence rate and robustness.

Future work will be devoted to designing combinations of DOM as visual features that can be used to control the trajectory of the camera in Cartesian space. Additionally, we intend to investigate more flexible DOM that can be used as visual features, such as Racah moments, etc.

ACKNOWLEDGMENTS

Thanks to Shuo Wang for providing language help and all our colleagues for providing all types of help during the preparation of this manuscript.

REFERENCES

- [1] K. Fathian, J. Jin, S.-G. Wee, D.-H. Lee, Y.-G. Kim, and N. R. Gans, "Camera relative pose estimation for visual servoing using quaternions," *Robotics and Autonomous Systems*, vol. 107, pp. 45–62, 2018.
- [2] M. Bakthavatchalam, O. Tahri, and F. Chaumette, "Improving moments-based visual servoing with tunable visual features," in *2014 IEEE international conference on robotics and automation (ICRA)*. IEEE, 2014, pp. 6186–6191.

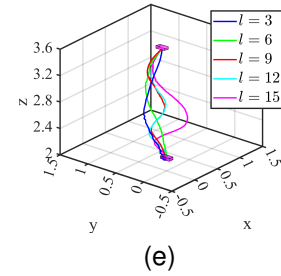
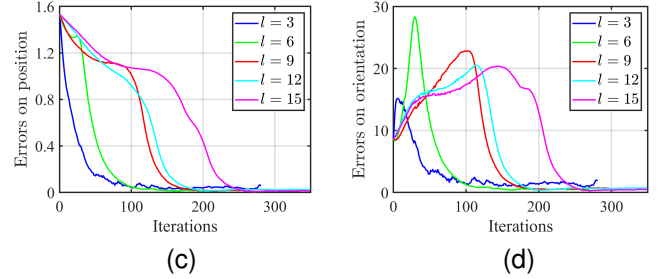
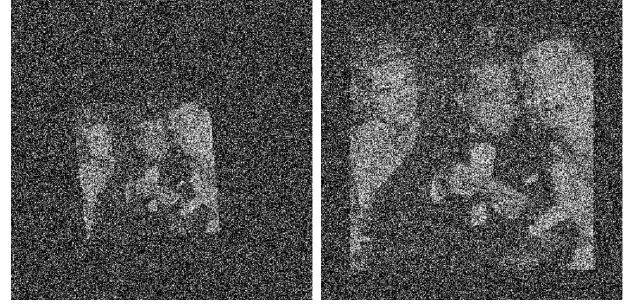


Fig. 26. Influence of DOM order in case of Gaussian noise ($\sigma^2 = 0.4$). (a) Initial image. (b) Desired image. (c) The position errors (in m). (d) The orientation errors (in $^\circ$). (e) The camera trajectories (in m).

- [3] V. D. Cong, "Visual servoing control of 4-dof palletizing robotic arm for vision based sorting robot system," *International Journal on Interactive Design and Manufacturing (IJIDeM)*, pp. 1–12, 2022.
- [4] H. Shi, G. Sun, Y. Wang, and K.-S. Hwang, "Adaptive image-based visual servoing with temporary loss of the visual signal," *IEEE Transactions on Industrial Informatics*, vol. 15, no. 4, pp. 1956–1965, 2018.
- [5] P. Serra, R. Cunha, T. Hamel, D. Cabecinhas, and C. Silvestre, "Landing of a quadrotor on a moving target using dynamic image-based visual servo control," *IEEE Transactions on Robotics*, vol. 32, no. 6, pp. 1524–1535, 2016.
- [6] H. Shi, J. Chen, W. Pan, K.-S. Hwang, and Y.-Y. Cho, "Collision avoidance for redundant robots in position-based visual servoing," *IEEE Systems Journal*, vol. 13, no. 3, pp. 3479–3489, 2018.
- [7] Y. Chen, X. Luo, B. Han, J. Jiang, and Y. Liu, "Closed-form camera pose and plane parameters estimation for moments-based visual servoing of planar objects," *International Journal of Advanced Robotic Systems*, vol. 19, no. 3, p. 17298806221099701, 2022.
- [8] S. Heshmati-alamdari, A. Eqtami, G. C. Karras, D. V. Dimarogonas, and K. J. Kyriakopoulos, "A self-triggered position based visual servoing model predictive control scheme for underwater robotic vehicles," *Machines*, vol. 8, no. 2, p. 33, 2020.
- [9] V. Lippiello, B. Siciliano, and L. Villani, "Position-based visual servoing in industrial multirobot cells using a hybrid camera configuration," *IEEE Transactions on Robotics*, vol. 23, no. 1, pp. 73–86, 2007.
- [10] M. Bakthavatchalam, O. Tahri, and F. Chaumette, "A direct dense visual servoing approach using photometric moments," *IEEE Transactions on Robotics*, vol. 34, no. 5, pp. 1226–1239, 2018.
- [11] C. Collewet, E. Marchand, and F. Chaumette, "Visual servoing set free

from image processing,” in *2008 IEEE International Conference on Robotics and Automation*. IEEE, 2008, pp. 81–86.

- [12] C. Collewet and E. Marchand, “Photometric visual servoing,” *IEEE Transactions on Robotics*, vol. 27, no. 4, pp. 828–834, 2011.
- [13] E. Marchand, “Subspace-based direct visual servoing,” *IEEE Robotics and Automation Letters*, vol. 4, no. 3, pp. 2699–2706, 2019.
- [14] S. Felton, P. Brault, E. Fromont, and E. Marchand, “Visual servoing in autoencoder latent space,” *IEEE Robotics and Automation Letters*, vol. 7, no. 2, pp. 3234–3241, 2022.
- [15] Q. Bateux and E. Marchand, “Histograms-based visual servoing,” *IEEE Robotics and Automation Letters*, vol. 2, no. 1, pp. 80–87, 2016.
- [16] X. Li, H. Zhao, and H. Ding, “Kullback-leibler divergence-based visual servoing,” in *2021 IEEE/ASME International Conference on Advanced Intelligent Mechatronics (AIM)*. IEEE, 2021, pp. 720–726.
- [17] N. Crombez, E. M. Mouaddib, G. Caron, and F. Chaumette, “Visual servoing with photometric gaussian mixtures as dense features,” *IEEE Transactions on Robotics*, vol. 35, no. 1, pp. 49–63, 2018.
- [18] E. Marchand, “Direct visual servoing in the frequency domain,” *IEEE Robotics and Automation Letters*, vol. 5, no. 2, pp. 620–627, 2020.
- [19] V. Lakshminarayanan and A. Fleck, “Zernike polynomials: a guide,” *Journal of Modern Optics*, vol. 58, no. 7, pp. 545–561, 2011.
- [20] R. Mukundan, S. Ong, and P. Lee, “Discrete vs. continuous orthogonal moments for image analysis,” in *Proceedings of the International Conference on Imaging Science, Systems, and Technology CISST*, July 2001, pp. 23–29.
- [21] R. Mukundan and K. R. Ramakrishnan, *Moment functions in image analysis-theory and applications*. Singapore: World Scientific, 1998.
- [22] H. Zhu, M. Liu, H. Shu, H. Zhang, and L. Luo, “General form for obtaining discrete orthogonal moments,” *IET image processing*, vol. 4, no. 5, pp. 335–352, 2010.
- [23] R. Mukundan, S. Ong, and P. A. Lee, “Image analysis by tchebichef moments,” *IEEE Transactions on image Processing*, vol. 10, no. 9, pp. 1357–1364, 2001.
- [24] P.-T. Yap, R. Paramesran, and S.-H. Ong, “Image analysis by krawtchouk moments,” *IEEE Transactions on image processing*, vol. 12, no. 11, pp. 1367–1377, 2003.
- [25] R. Mukundan, “Some computational aspects of discrete orthonormal moments,” *IEEE Transactions on image processing*, vol. 13, no. 8, pp. 1055–1059, 2004.
- [26] P.-T. Yap, R. Paramesran, and S.-H. Ong, “Image analysis using hahn moments,” *IEEE transactions on pattern analysis and machine intelligence*, vol. 29, no. 11, pp. 2057–2062, 2007.
- [27] A. F. Nikiforov and V. B. Uvarov, *Special functions of mathematical physics*. Springer, 1988, vol. 205.
- [28] P. T. Yap, “Moments-based pattern analysis: theory and applications,” Ph.D. dissertation, Jabatan Kejuruteraan Elektrik, Fakulti Kejuruteraan, Universiti Malaya, 2007.
- [29] C. François and S. Hutchinson, “Visual servo control part i: Basic approaches,” *IEEE Robot. Autom. Mag.*, vol. 13, pp. 82–90, 2006.
- [30] E. Malis, “Improving vision-based control using efficient second-order minimization techniques,” in *IEEE International Conference on Robotics and Automation, 2004. Proceedings. ICRA’04. 2004*, vol. 2. IEEE, 2004, pp. 1843–1848.

VII. BIOGRAPHY SECTION



Yuhao Chen received the Ph.D. degree in mechanical engineering from the Beijing Institute of Technology, Beijing, China, in 2022, and received the B.S. degree in mechanical engineering from the Taiyuan University of Technology, Taiyuan, China, in 2016. His research interests include visual servoing, robotic, mobile manipulation, and robot dynamics.



Max Q.-H. Meng (Fellow, IEEE) received the Ph.D. degree in electrical and computer engineering from the University of Victoria, Victoria, BC, Canada, in 1992.

He was with the Department of Electrical and Computer Engineering, University of Alberta, Edmonton, AB, Canada, where he served as the Director of the Advanced Robotics and Teleoperation Laboratory, holding the positions of an Assistant Professor, an Associate Professor, and a Professor in 1994, 1998, and 2000, respectively. In 2001, he joined The Chinese University of Hong Kong, where he served as the Chairman of the Department of Electronic Engineering, holding the position of a Professor. He is affiliated with the State Key Laboratory of Robotics and Systems, Harbin Institute of Technology, and is the Honorary Dean of the School of Control Science and Engineering, Shandong University, China. He is currently with the Department of Electronic and Electrical Engineering, Southern University of Science and Technology, on leave from the Department of Electronic Engineering, The Chinese University of Hong Kong, Hong Kong SAR, China, and also with the Shenzhen Research Institute, The Chinese University of Hong Kong, Shenzhen, China. His research interests include robotics, medical robotics and devices, perception, and scenario intelligence. He has published about 600 journal and conference papers and led more than 50 funded research projects to completion as PI.

Dr. Meng is a recipient of the IEEE Millennium Medal. He has served as an editor for several journals and also as the General and Program Chair for many conferences, including the General Chair of IROS 2005 and the General Chair of ICRA 2021. He is an Elected Member of the Administrative Committee of the IEEE Robotics and Automation Society. He is a Fellow of the Canadian Academy of Engineering and HKIE.



Li Liu received his Ph.D. degree in Biomedical Engineering from the University of Bern, Switzerland, and then worked as a postdoctoral fellow at the University of Bern and the Chinese University of Hong Kong. He held the position of assistant professor in the School of Biomedical Engineering at Shenzhen University since 2016. In 2019 he joined CUHK as a faculty member. He has served as Program and Publication Chair of many international conferences including Publication Chair of IEEE ICIA 2017, 2018 and Program Chair of ROBIO 2019, Video Chair of IEEE ICRA 2021. He served as Associate Editor of Biomimetic Intelligence and Robotics (BIOB) since 2021. He is a recipient of the Distinguished Doctorate Dissertation Award, Swiss Institute of Computer Assisted Surgery (2016), the MICCAI Student Travel Award (2014) and the Best Paper Award of IEEE ICIA (2009). His current interests focus on the interface of surgical robotics, in-situ sensing and medical imaging, and to develop robotic-enabled medical imaging as well as image-guided robotic surgical systems, where ultrasound, photoacoustic sensing/imaging and endoscopic OCT are three major modalities to be investigated and incorporated with minimally invasive surgical robotics.